System Implementation for the Soft Start Operation of a Doubly-Fed Induction Motor

Knapoj Chaimanekorn and **Warachart Suwan-ngam**†, Non-members

ABSTRACT

This research aims at system implementation for the soft start operation of a doubly-fed induction motor (DFIM) based on stator flux vector control. In this paper, the theory is briefly discussed. The simulation is performed using PLECS software to validate the hypothesis. A 5 kW wound rotor induction motor (WRIM) mechanically coupled with a simulated load is setup for the experiment. The STM32F407 microcontroller is applied to control the experimental system. Moreover, the Modbus protocol is applied for communication between the microcontroller and the computer using RS485 standard. The problem about rotor angle correction before enabling the MSC, which does not appear in the simulation, is seriously discussed. The experimental results do substantiate the proposed method and can be practically applied to the real system.

Keywords: System Implementation, Doubly-fed Induction Motor, Soft Start, Stator Flux Vector Control

NOMENCLATURE

L_{sl}, L_{rl}	Stator and rotor leakage inductances.
L_s, L_r	Stator and rotor self-inductances.
L_m	Three-phase magnetizing inductance.
$L_{rl}^{'}$	Referred rotor leakage inductance.
R_s, R_r	Stator and rotor resistances.
$R_r^{'}$	Referred rotor resistance.
τ_s, τ_r	Stator and rotor time constant.
τ_f	Filter time constant.
σ	Total leakage factor.
N_s, N_r	Number of stator and rotor turns.
a	Stator-rotor turn ratio.
s	Slip.
P	Number of poles.
P_s, P_r	Stator and rotor active power.
Q_s	Stator reactive power.
$\vec{i}_s, \vec{i}_r$	Stator and rotor current vectors.
$\vec{i}_{ms}$	Stator magnetizing current vector.
$\vec{v}_r^{'}, \vec{i}_r^{'}$	Referred rotor voltage and current vectors.
$\vec{\lambda}_s$	Stator flux vector.
$\vec{v}_s^e, \vec{v}_r^{'e}$	Stator and referred rotor voltage vectors in stator flux reference frame.
$\vec{i}_s^e, \vec{i}_r^{'e}$	Stator and referred rotor current vectors in stator flux reference frame.
$\vec{i}_s^s$	Stator current vector in stationary reference frame fixed to stator.
$\vec{i}_{ms}^e$	Stator magnetizing current vector in stator flux reference frame.
$\vec{\lambda}_s^{sv}$	Stator flux vector in stationary reference frame fixed to stator calculated from voltage model.
$\vec{\lambda}_s^{si}$	Stator flux vector in stationary reference frame fixed to stator calculated from current model.
$\vec{\lambda}_s^e, \vec{\lambda}_r^{'e}$	Stator and referred rotor flux vectors in stator flux reference frame.
i_{sd}^e, i_{sq}^e	D-axis and Q-axis stator currents in stator flux reference frame.
$i_{rd}^{'e}, i_{rq}^{'e}$	D-axis and Q-axis rotor currents in stator flux reference frame.
$\lambda_{sd}^e, \lambda_{sq}^e$	D-axis and Q-axis Stator flux linkages in stator flux reference frame.
ω_e	Stator flux speed, Synchronous speed.
ω_r, ω_{rm}	Rotor electrical and mechanical angular speeds.
ω_{sl}	Slip speed.
τ_m	Mechanical Time constant.
T_e	Electromagnetic torque.
T_L	Load torque.
B	Viscous friction coefficient.
K_a, K_b	Series gain and Inflection frequency.
V_{sb}, I_{sb}	Base Voltage and Current.
ω_{bm}	Base mechanical angular speed.

Manuscript received on April 24, 2024; revised on July 9, 2024; accepted on August 2, 2024. This paper was recommended by Associate Editor Chainarin Ekkaravarodome.

The authors are with School of Engineering, King Mongkut's Institute of Technology Ladkrabang, Ladkrabang, Bangkok, Thailand.

†Corresponding author: warachart.su@kmitl.ac.th

Digital Object Identifier: 10.37936/ecti-eec.2024223.253804

1. INTRODUCTION

A doubly-fed induction motor (DFIM) consists of a wound rotor induction machine (WRIM) having rotor connected to the back-to-back converter as can be found in a doubly-fed induction generator (DFIG) discussed in [1-6]. These converters are constructed from two PWM converters connected in back-to-back. The converter

at the rotor side is called the machine-side converter (MSC) which is responsible for control of the DFIM. While the rotor is connected to the MSC, the stator is generally connected to the constant voltage constant frequency source. Therefore, the DFIM can also be called a doubly-excited induction motor. The functions of the MSC consists of active and reactive power control of the DFIM. The active power control function is in the form of either speed or torque control. Besides, for reactive power control function, the MSC can behave as an exciter of the wound field synchronous motor (WFSM). The major application of the DFIM is in areas of pump and marine [7-16], though it requires more than one converter. Various research studies have introduced different starting methods based on the conventional topology [8-18, 31-33].

Operation of the DFIM requires a start-up method to accelerate the rotor from a standstill. Various methods have been proposed, and some are widely used today. They require circuit reconfiguration from start-up to normal operation. The most effective method uses the MSC to control the rotor circuit while short-circuiting the stator circuit, as illustrated in Fig. 1a [8-15]. Two induction motor control methods are applied to the MSC: constant V/F and stator-flux vector control. This approach enables the DFIM to start and accelerate to a specific speed in the sub-synchronous speed region. Once the speed is stabilized, the MSC is stopped, and the circuit is reconfigured as depicted in Fig.1b for grid synchronization process. As performed in the DFIG, the MSC resumes operation and the contactor K1 is kept open during this interval. K1 is then closed once the DFIM is completely synchronized to the grid, and the DFIM can accelerate and operate under stator flux vector control. An alternative topology requires an initial

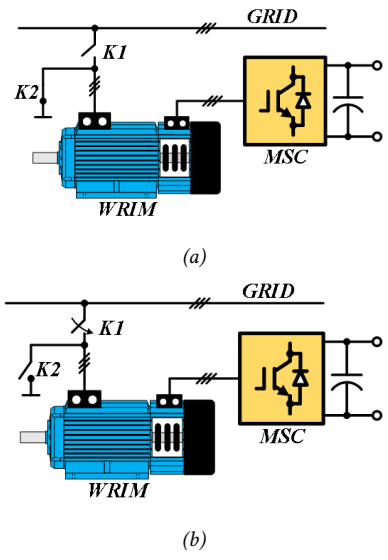

***Fig. 1**: Start-up Topologies for the DFIM Based on Driving the Rotor Circuit (a) Start-up and Acceleration Periods and (b) Grid Synchronization and Normal Operation Period.*

configuration by short-circuiting the rotor circuit and connecting the MSC to the stator circuit, as illustrated in Fig. 2a [10,16]. In this configuration, the MSC drives the DFIM based on rotor flux vector control as applied to a conventional stator fed induction motor. The motor can start and accelerate to a designated speed as in the previous method. Once the motor reaches the desired speed, the MSC is temporarily stopped, and the circuit is reconfigured as depicted in Fig. 2b. The contactor K1 remains open for the grid synchronization process. After grid synchronization, K1 is closed, and the DFIM is driven based on stator flux vector control.

A notable aspect of these two approaches is the necessity to temporarily halt the MSC and reconfigure the circuit prior to grid synchronization. During this interval, the DFIM operates without control, leading to speed deceleration depending on the mechanical time constant of the system. Nonetheless, most applications found in several research studies focused on a high inertia system, so the speed change is insignificant. A

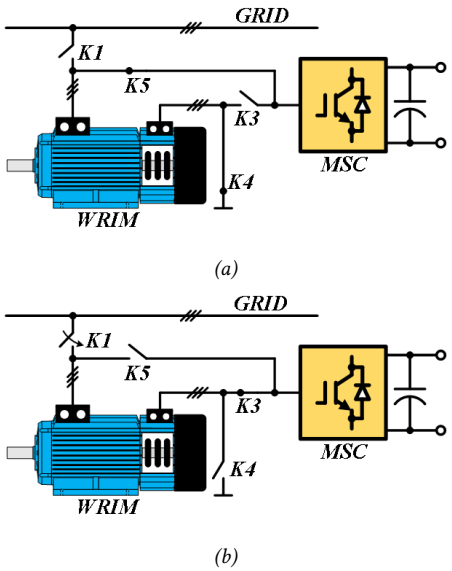

***Fig. 2**: Start-up Topologies for the DFIM Based on Driving the Stator Circuit (a) Start-up and Acceleration Period and (b) Grid Synchronization and Normal Operation Period.*

switched doubly-fed induction machine proposed by A. Banerjee *et al.* has been applied for a start-up procedure. This scheme involves the application of a DC voltage source to the stator as illustrated in Fig.3. During startup and acceleration, the DFIM operates as a WFSM driven the MSC via rotor circuit. The stator flux vector control is applied to the MSC as discussed in [17,18]. This approach required switching from a DC source to an AC source, and the results indicate a smooth speed transition.

The DFIM start-up strategy involves using a stator-connected converter, creating a dual converter topology [19-30]. This setup enables four-quadrant operation through the control of the stator-side converter (SSC), which handles the start-up process, while the MSC controls the rotor flux. Various controls have been

proposed to synchronize SSC and MSC operations.

Start-up methods using the MSC have also been proposed [31-33], but they need precise control until the speed reaches a certain level, at which point the system switches to grid voltage or stator flux vector control. This paper presents system implementation

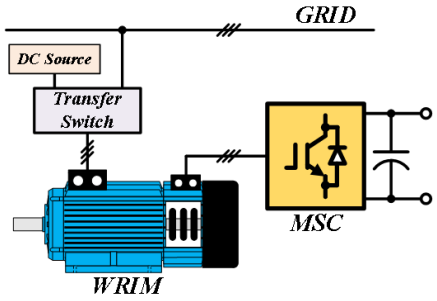

***Fig. 3**: Start-up Topologies for the DFIM Based on Switched Supplies.*

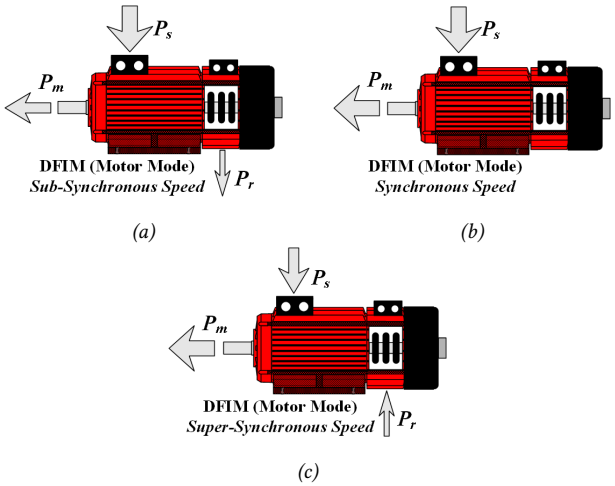

***Fig. 4**: Active Power Flow Diagram of a DFIM for Operation in Different speed Regions, (a) Sub-Synchronous Speed, (b) Synchronous Speed, and (c) Super-Synchronous Speed.*

of the DFIM for startup and acceleration based on stator flux vector control without either change of circuit configuration or control method. The issues occur in practice are also addressed. The paper starts with a discussion of the stator flux vector control of the DFIM in Section 2. This section includes explanation of the stator flux vector estimation and control of the stator reactive power of the DFIM. The control loop design is also included in this section. Section 3 then presents the operating sequence to achieve the proposed soft start operation for the DFIM. The simulation using PLECS software, and the experimental setup are discussed in Section 4. The simulation and experimental results are then presented and discussed in Section 5. Finally, the conclusion is proposed in Section 6.

2. A DOUBLY-FED INDUCTION MOTOR

A DFIM with a variable voltage variable frequency source connected to the rotor can operate in sub-synchronous speed, synchronous speed, and super synchronous speed regions. It can be graphically explained as shown in Fig. 4 together with the rotor power equation as described in equation (1),

$$P_r = -sP_s. \tag{1}$$

A four-quadrant converter is required for connection to the rotor. The most applicable topology is shown in Fig. 5. The back-to-back converters are connected to the rotor of the WRIM. However, in this paper, only the operation of the MSC is considered. For motor

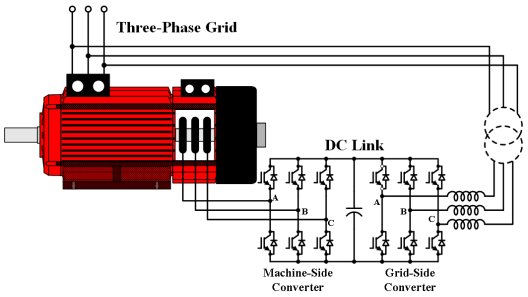

***Fig. 5**: Conventional Topology of a DFIM.*

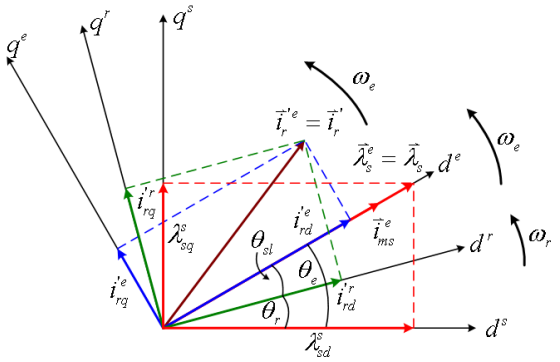

***Fig. 6**: Vector Diagram of the Rotor Current under Stator Flux Vector Control of the DFIM.*

application, regardless of the restriction of the converter size, the WRIM can operate up to 2 times of the base speed without field weakening. The commonly used control for the DFIM is the stator flux vector control which is discussed in the next sub-section.

2.1 Stator Flux Vector Control

Control of the DFIM based on stator flux vector control requires knowledge of the reference frame theory and the stator flux vector estimation. The vector diagram of the rotor current vector and the necessary reference frames is shown in Fig. 6,

The stator flux vector in general form is the function of stator current and rotor current vectors as described in

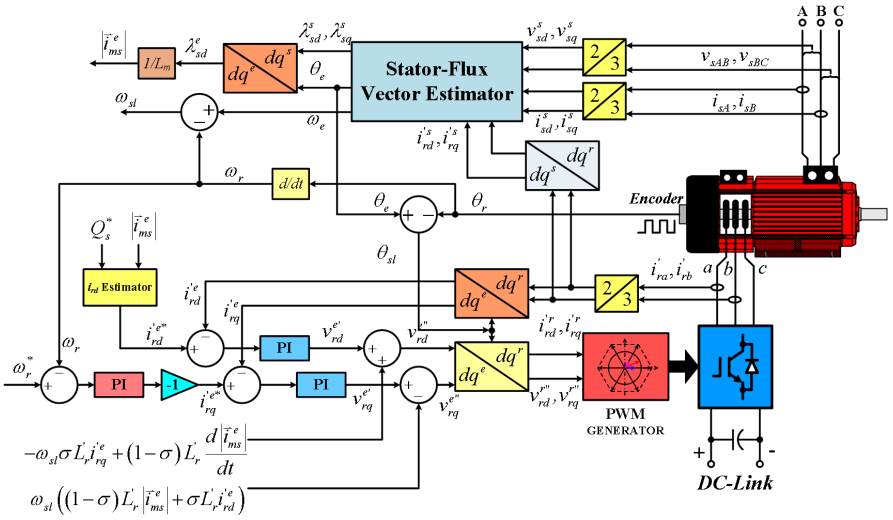

***Fig. 7**: Control Diagram of the DFIM.*

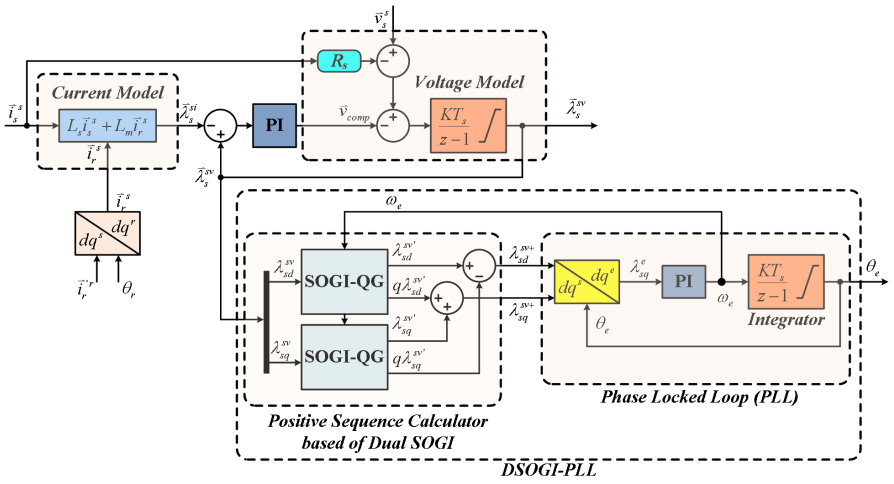

***Fig. 8**: Stator Flux Vector Estimation Block Diagram with DSOGI-PLL.*

equation (2). Likewise, it can also be written in the form of the stator magnetizing current as described in equation (3) [1,2],

$$\vec{\lambda}_s = L_s \vec{i}_s + L_m \vec{i}'_r \tag{2}$$

$$\vec{\lambda}_s = L_m \vec{i}_{ms}. \tag{3}$$

The stator current vector must be arranged into the form of $\vec{i}^{\,e}_{ms}$ and $\vec{i}'^{\,e}_r$ as shown in equation (4),

$$\vec{i}^{\,e}_s = \frac{L_m}{L_s}(\vec{i}^{\,e}_{ms} - \vec{i}'^{\,e}_r) \tag{4}$$

The rotor and stator voltage vector equations in the stator flux reference frame are presented in equations (5) and (6) respectively.

$$\vec{v}'^{\,e}_r = R'_r \vec{i}'^{\,e}_r + \frac{d\vec{\lambda}'^{\,e}_r}{dt} + j(\omega_e - \omega_r)\vec{\lambda}'^{\,e}_r \tag{5}$$

$$\vec{v}^{\,e}_s = R_s \vec{i}^{\,e}_s + \frac{d\vec{\lambda}^{\,e}_s}{dt} + j\omega_e \vec{\lambda}^{\,e}_s \tag{6}$$

The 1^{st} order differential equation form of equations (5) and (6) are shown in equations (7) and (8) respectively,

$$\sigma\tau'_r \frac{d\vec{i}'^{\,e}_r}{dt} + \vec{i}'^{\,e}_r = \frac{\vec{v}'^{\,e}_r}{R'_r} - j\omega_{sl}\sigma\tau'_r \vec{i}'^{\,e}_r - (1-\sigma)\tau'_r \left(\frac{d\vec{i}^{\,e}_{ms}}{dt} + j\omega_{sl}\vec{i}^{\,e}_{ms} \right) \tag{7}$$

$$\tau_s \frac{d\vec{i}^{\,e}_{ms}}{dt} + \vec{i}^{\,e}_{ms} = \tau_s \frac{\vec{v}^{\,e}_s}{L_m} + \vec{i}'^{\,e}_r - j\omega_e \tau_s \vec{i}^{\,e}_{ms} \tag{8}$$

where $\sigma = 1 - \frac{L_m^2}{L_s L'_r}$, and $\omega_{sl} = \omega_e - \omega_r$.

The torque, reactive power equations as well as mechanical dynamic equation are presented in equations

(9)-(11) respectively, and control diagram is depicted in Fig. 7,

$$T_e = -\frac{P}{2}\frac{3}{2}\frac{L_m^2}{L_s}\left|\vec{i}^{\,e}_{ms}\right| i'^{e}_{rq} \tag{9}$$

$$Q_s = \omega_e \frac{P}{2}\frac{3}{2}\frac{L_m^2}{L_s}\left|\vec{i}^{\,e}_{ms}\right|\left(\left|\vec{i}^{\,e}_{ms}\right| - i'^{e}_{rd}\right) \tag{10}$$

$$\tau_m \frac{d\omega_{rm}}{dt} + \omega_{rm} = T_e - T_L \tag{11}$$

2.2 Stator Flux Vector Estimation

The most important part of vector control is the reference frame estimation. Therefore, stator flux vector estimation is mandatory. The voltage model is an ideal method for estimating the stator flux due to its simplicity and less parameter dependent. However, this method does suffer from a small DC offset causing an overflow of the integrating results. Several methods are proposed to solve this problem and can be categorized into two groups: open loop observer and closed loop observer [34]. One of the simple methods is the low cut-off frequency low pass filter method. However, the adaptive method based on voltage and current models is adopted in this paper for better performance [34, 35]. The equations for the stator flux vector estimation using voltage and current models are described in equations (12) and (13) respectively.

$$\vec{\lambda}^{sv}_s = \int (\vec{v}^{\,s}_s - R_s \vec{i}^{\,s}_s)dt \tag{12}$$

$$\vec{\lambda}^{si}_s = L_s \vec{i}^{\,s}_s + L_m \vec{i}^{\,'s}_r \tag{13}$$

The voltage model is used as the reference model, and the current model is applied to calculate the compensating voltage as described in equation (14),

$$\vec{v}_{comp} = K_p(\vec{\lambda}^{sv}_s - \vec{\lambda}^{si}_s) + K_i \int (\vec{\lambda}^{sv}_s - \vec{\lambda}^{si}_s)dt \tag{14}$$

where $K_p = \omega_1 + \omega_2$, $K_i = \omega_1 \cdot \omega_2$, ω_1 = 2-5 rad/s and ω_2 = 20-30 rad/s [35].

The stator flux vector can be calculated as follows,

$$\begin{aligned}\vec{\lambda}^{sv}_s &= \int(\vec{v}^{\,s}_s - R_s \vec{i}^{\,s}_s - \vec{v}_{comp})dt \\ &= \int \vec{e}_{s\_comp}dt\end{aligned} \tag{15}$$

where $\vec{e}_{s\_comp}$ is a compensated induced voltage and, $\vec{v}_{comp}$ is a compensating voltage from (14).

The process of stator flux vector estimation can be depicted as shown in Fig.8. However, in practice, the three-phase grid is hardly balanced, causing oscillation in the stator flux estimated, as well as oscillation in the stator flux angular frequency and position while using only the general dq-PLL. Therefore, in this paper, a dual second-order generalized integrator phase locked loop (DSOGI-PLL) is applied to provide the smooth angular frequency and position estimated based on the positive sequence extraction as described in [36].

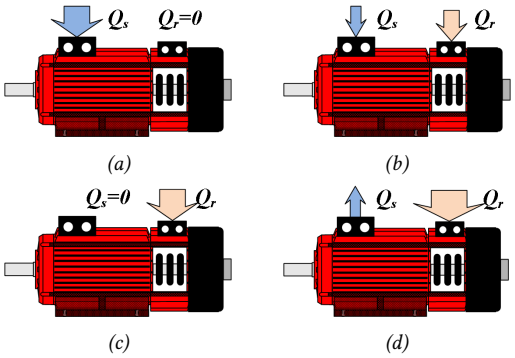

***Fig. 9**: Reactive Power Flow Diagram of a DFIM for, (a) Stator Excitation, (b) Under Excitation, (c) Normal Excitation, and (d) Over Excitation.*

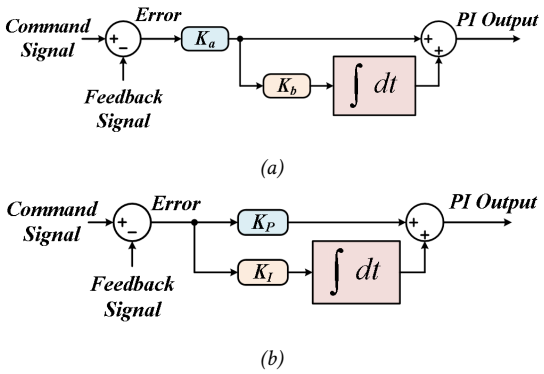

***Fig. 10**: PI Controller Structures (a) Series (b) Parallel.*

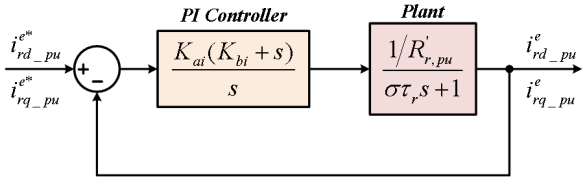

***Fig. 11**: Torque Control Loop.*

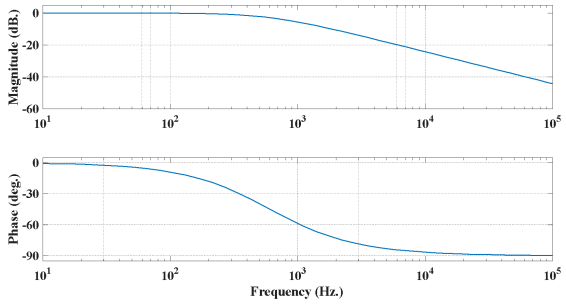

***Fig. 12**: The Bode Plot for the Closed-Loop Transfer Function of the Current Loop.*

2.3 Stator Reactive Power Control

From the stator voltage vector equation in equation (8), considering only equation in d-axis, it can be arranged in the form of the differential equation of the

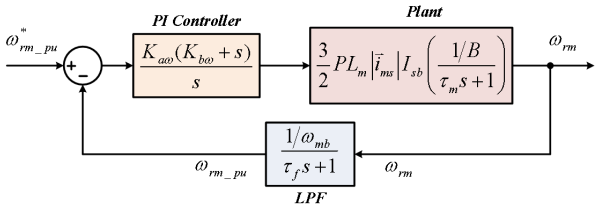

***Fig. 13**: Speed Control Loop.*

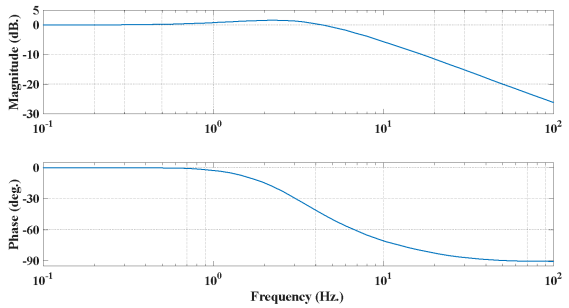

***Fig. 14**: The Bode Plot for the Closed-Loop Transfer Function of the Speed Loop.*

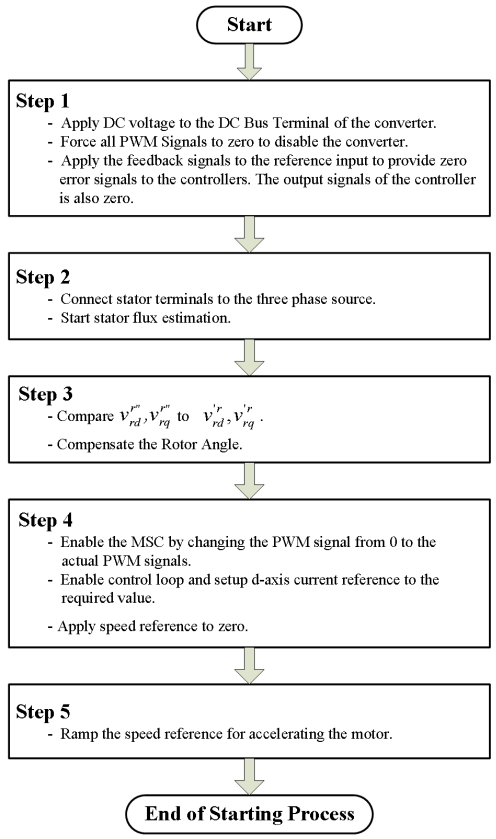

***Fig. 15**: Flowchart Showing the Operating Sequence for the Soft Start Operation of the DFIM.*

$\vec{i}^{\,e}_{ms}$as shown in equation (16),

$$\tau_s \frac{d\left|\vec{i}^{\,e}_{ms}\right|}{dt} + \left|\vec{i}^{\,e}_{ms}\right| = \tau_s \frac{v^e_{sd}}{L_m} + i'^{e}_{rd}. \tag{16}$$

***Table 1**: Controller Gains and Bandwidth of the Current and Speed Control Loops.*

Controller Parameters	Current Loop	Speed Loop
K_a	2.5	2
K_b	200 s^{-1}	10 s^{-1}
Bandwidth	629.58 Hz.	7.15 Hz.

This equation indicates the that the stator flux linkage is the function of both d-axis stator and d-axis rotor currents. Moreover, the DFIM is controlled by the MSC at the rotor circuit, therefore, the MSC can operate as an exciter of a WFSM for excitation.

Hence, the stator reactive power can be managed by controlling the MSC. As shown in equation (16), the unit step response of the $\vec{i}^{\,e}_{ms}$ to a step change in either v^e_{sd} or i'^{e}_{rd} is the 1^{st} order response with time constant equal to the stator time constant,τ_s. At steady state, the stator magnetizing current depends on either V^e_{sd}or I'^{e}_{rd}.as described in equation (17),

$$\begin{aligned}\left|\vec{I}^{\,e}_{ms}\right| &= \tau_s \frac{V^e_{sd}}{L_m} + I'^{e}_{rd} \\ &= \frac{L_s}{L_m} I^e_{sd} + I'^{e}_{rd}.\end{aligned} \tag{17}$$

The stator reactive power control can be categorized into 4 cases, stator excitation, under excitation, normal excitation and over excitation. All reactive power flow diagrams are depicted in Fig. 9.

2.4 Control-Loop Design

The series PI controller structure is used in this research. Its structure is shown in Fig. 10a while the parallel structure is shown in Fig. 10b. The transfer function, $G_c(s)$ of the series PI controller is shown in equation (18),

$$G_c(s) = K_a + \frac{K_a K_b}{s}. \tag{18}$$

while K_a is the series gain and K_b is the inflection frequency [37].

The benefit of the series topology is the ease of locating the zero of the controller and adjusting the bandwidth of the closed loop system. Since K_a is used to adjust the gain, so the bandwidth consequently adjusted. Meanwhile, K_b affects only the inflection frequency. It does not increase the gain at high frequency.

The relationship between K_a, K_b for the series structure and K_P, K_I for the parallel structure is shown in equations (19) and (20) respectively,

$$K_P = K_a, \tag{19}$$

$$K_I = K_a K_b. \tag{20}$$

Both current and speed controllers are designed in s-domain. Beginning with the current control loop,

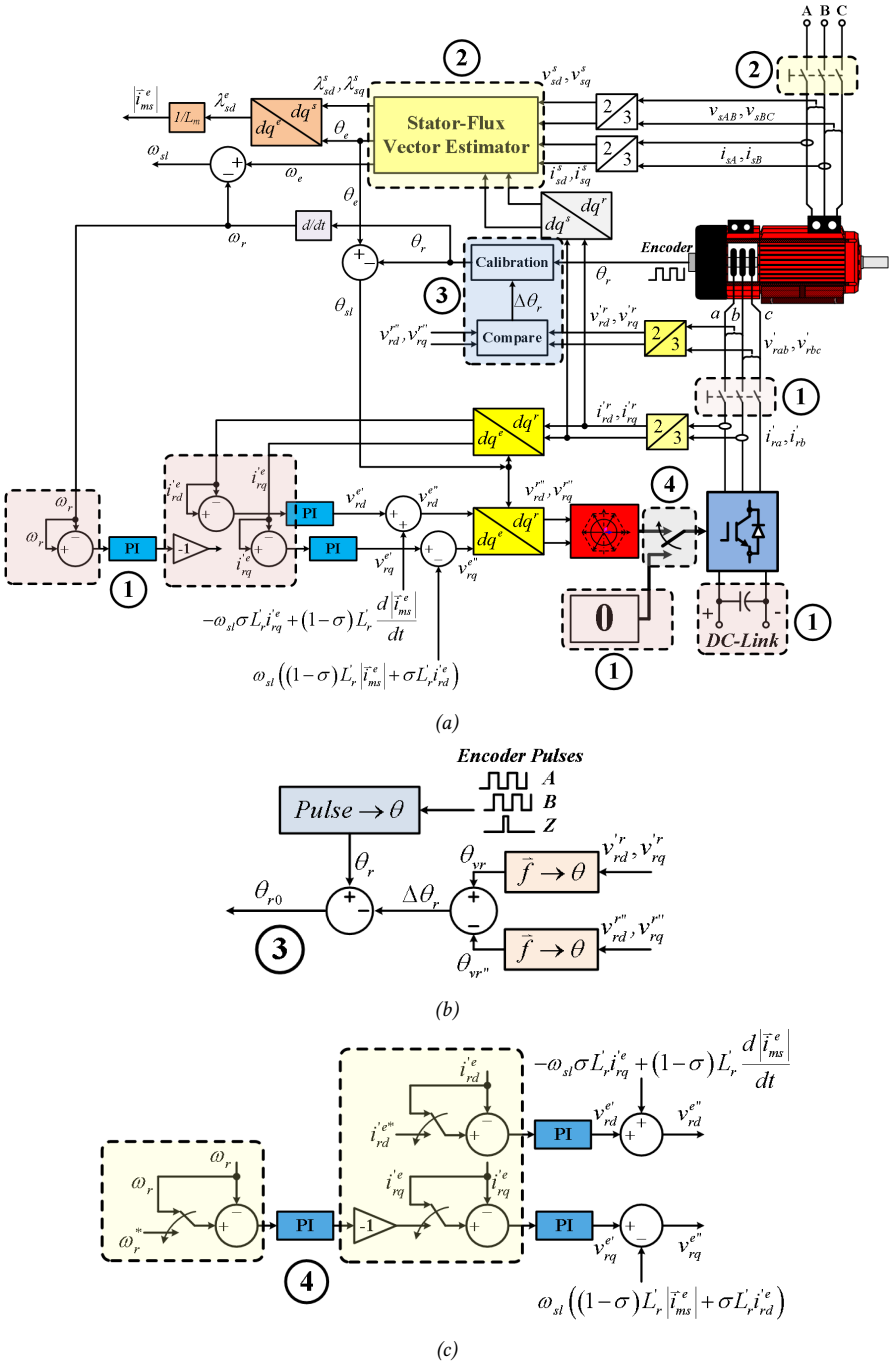

***Fig. 16**: Control Diagram Showing (a) the Operating Sequence for the Soft Start Operation from Step 1 to Step 4,(b) the Re-Calibration of the Rotor Angle, and (c) Change in Controller Reference at Step 4.*

***Table 2**: Parameters of a WRIM.*

Parameter	Value	Unit	Parameter	Value	Unit
Stator Rated Voltage	400	V	Stator Resistance	1.0972	Ω
Rotor Rated Voltage	200	V	Referred Rotor Resistance	2.0250	Ω
Stator Rated Current	9.7	A	Stator Self Inductance	0.203642	H
Rotor Rated Current	11.4	A	Referred Rotor Self Inductance	0.203642	H
Base Frequency	50	Hz.	Magnetizing Inductance	0.195853	H
Base Speed	1500	rpm.	Moment of Inertia	0.018	Kg-m^2
Number of Poles	4	Poles	Viscous Friction Coefficient	0.008242	N-m s/Rad
Stator-Rotor Turn Ratio	2		DC Bus Voltage	300	V

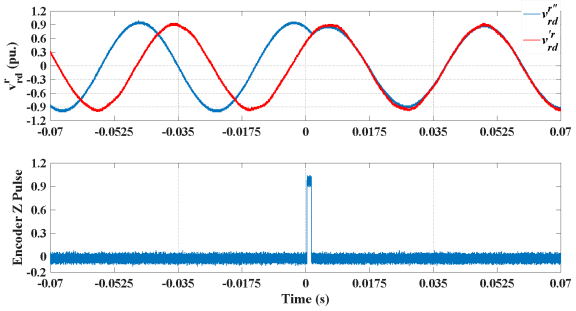

***Fig. 17**: Experimental Results Showing the Waveform of the D-Axis Component of the Measured Rotor Voltage and the Controller Command Voltage (top) and the Z-Pulse (bottom) during Appearance of the Z-Pulse.*

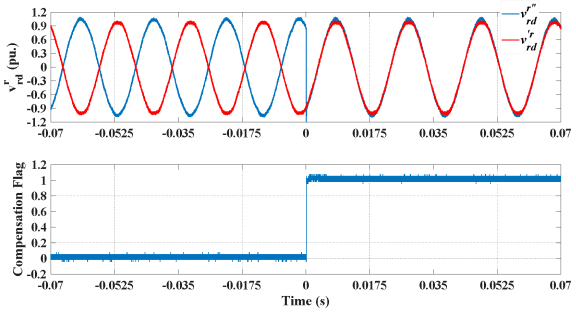

***Fig. 18**: FExperimental Results Showing the Waveform of the D-Axis Component of the Measured Rotor Voltage and the Controller Command Voltage (top) and the Compensation Flag (bottom) during Enabling the Compensation Process.*

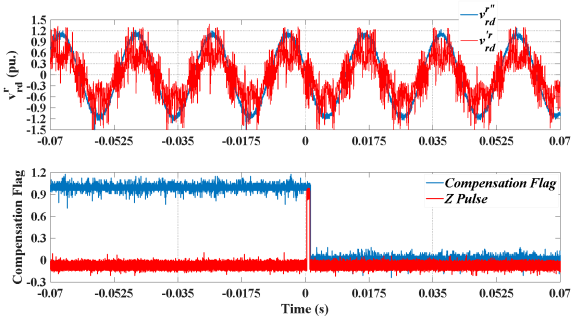

***Fig. 19**: Experimental Results Showing the Waveform of the D-Axis Component of the Measured Rotor Voltage and the Controller Command Voltage (top) and the Z-Pulse and Compensation Flag (bottom) during Appearance of the Z-Pulse.*

the plant transfer function (rotor circuit) is described in equation (21),

$$G_i(s) = \frac{V_{sb}}{I_{sb}} \frac{1/R_r'}{\sigma\tau_r s+1} = \frac{1/R_{r,pu}'}{\sigma\tau_r s+1} \quad . \tag{21}$$

With the controller transfer function in equation (18), the closed loop block diagram is shown in Fig.11. From Fig.11, K_{ai} and K_{bi} are the K_a and K_b for current control loop. The controller gains as well as the bandwidth of both current and speed loops are shown in Table 1. The frequency response for the current control loop is shown in Fig. 12, In the case of the speed control loop, the plant transfer function is described in equation (22),

$$G_m(s) = \frac{3}{2} P L_m \left|\vec{i}_{ms}\right| I_{sb} \frac{1/B}{\tau_m s + 1}. \tag{22}$$

Since the speed is synthesized from position acquired from the encoder pulses, the speed waveform has a step shape which is not suitable for the control system. It is required to be filtered by a discrete low-pass filter before applying to the other processes of the operation. For the sake of simplicity, feedback path of the speed loop is replaced by the 1^{st} low-pass filter having cut-off frequency at 40Hz. The transfer function is illustrated in (23),

$$G_f(s) = \frac{1/\omega_{bm}}{\tau_f s + 1}. \tag{23}$$

The closed loop block diagram is illustrated in Fig. 13 following equations (18), (22), and (23). From Fig.13, $K_{a\omega}$ and $K_{b\omega}$ are the K_a and K_b for speed control loop. The closed loop response of the speed control loop is slightly underdamped with the damping ratio equals to 0.9. The frequency responses for the speed control loop are shown in Fig. 14,

3. PROPOSED SOFT START OPERATION

This section mainly focuses on detail explanation about the implementation of the proposed soft start method based on control of the MSC. According to the operating mode, the DFIM generally start from standstill. The converter rating must be able to handle rated rotor power. The operating procedure is arranged as shown in the flowchart in Fig. 15.

The operating diagram following the flowchart is depicted in Fig.16. There are 5 steps for the soft start operation. The first 4 steps are depicted in Fig.16a while the re-calibration process is shown in Fig.16b, and the last step is shown in Fig.16c. Each step is labeled by the number in the circle.

The 1^{st} step: The MSC is first disable by forcing all switches to OFF. The DC bus is then energized by a DC voltage source. Meanwhile, the reference signal of each controller is set to the feedback signal of each controller. This technique is used to prevent saturation of each controller by forcing zero error to the controller. After all are set the rotor circuit is connected to the converter. There is no current flow between the rotor and the converter.

The 2^{nd} Step: The stator must be connected to a three-phase source. This connection is required to energize the DFIM. The stator flux vector estimation process is later performed after the stator currents reach a steady

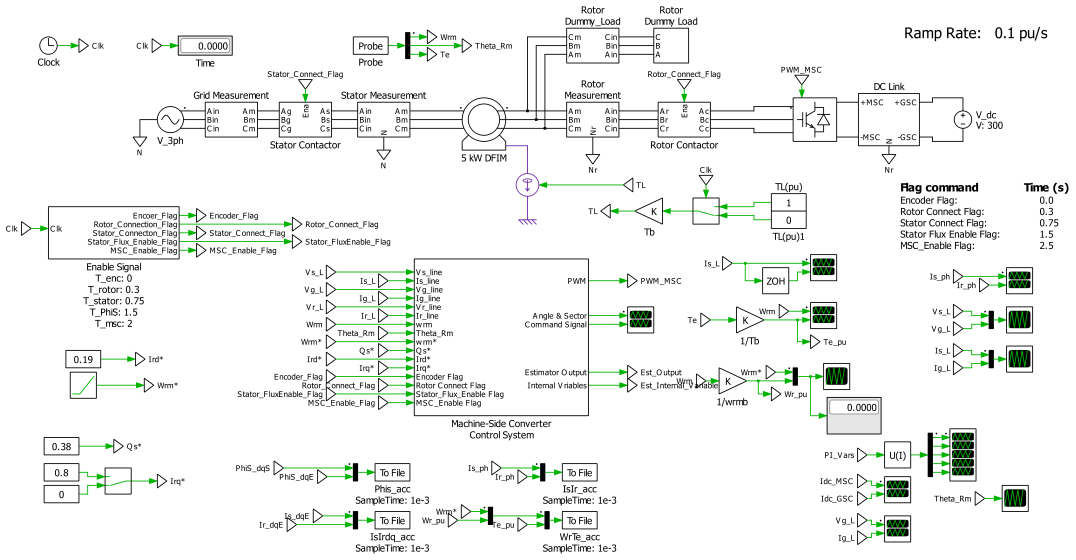

***Fig. 20**: Simulation Diagram for the Proposed Soft Start Operation Based on Stator Flux Vector Control.*

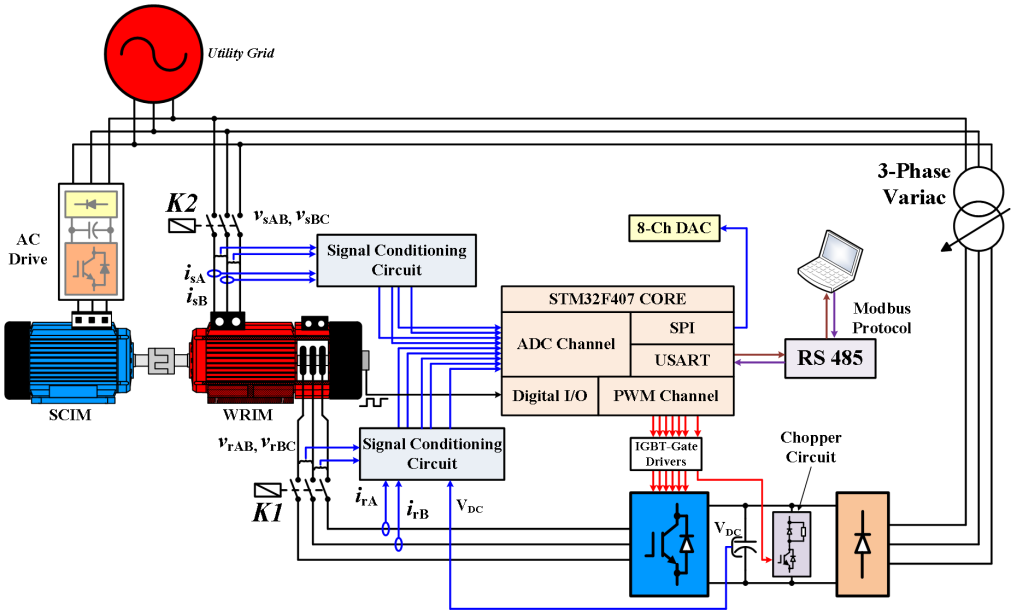

***Fig. 21**: Experimental Diagram for the Proposed Soft Start Operation Based on Stator Flux Vector Control.*

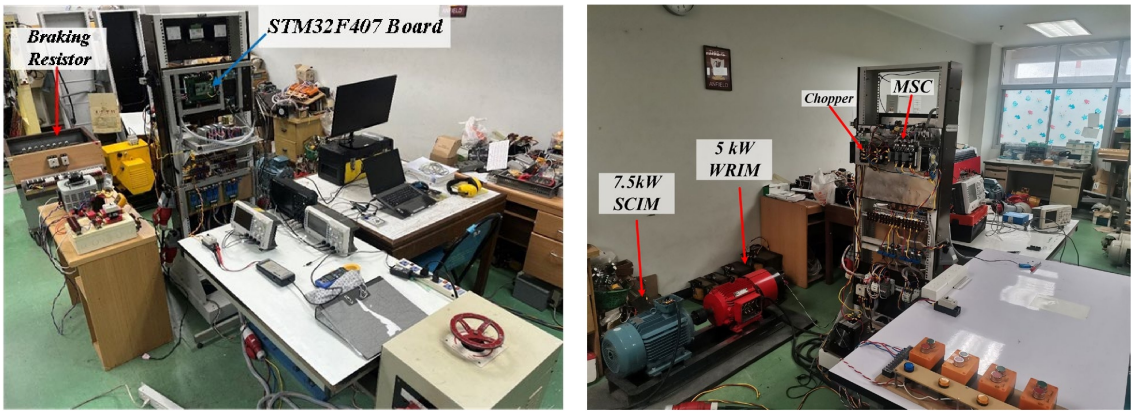

***Fig. 22**: Experimental System.*

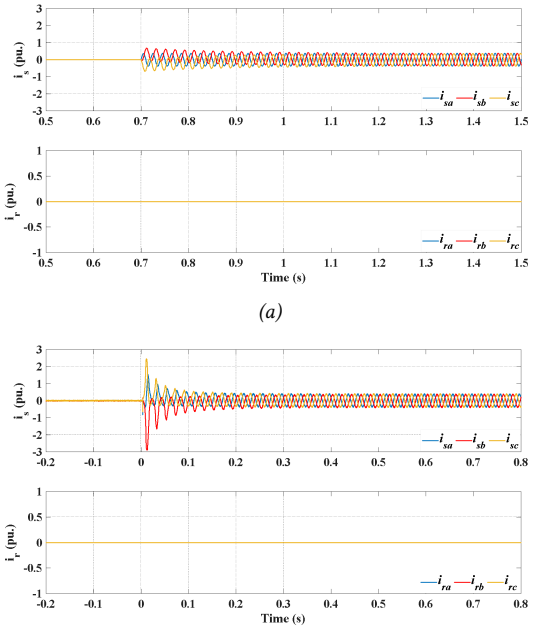

(a)

(b)

***Fig. 23**: (a) Simulation and (b) Experimental Results Showing the Waveforms of (Top) the Stator Current and (Bottom) the Rotor Current while Connecting the Stator to the Grid.*

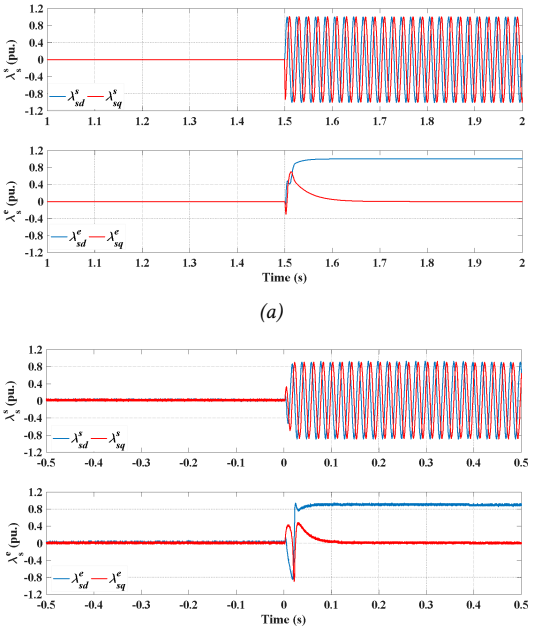

(a)

(b)

***Fig. 24**: (a) Simulation and (b) Experimental Results Showing the Waveforms of the Stator Flux Linkage in the Stationary Reference Frame (Top) and the Stator Flux Reference Frame (Bottom) while Enabling the Stator Flux Estimation.*

state. During this step, the converter command voltages in stator flux reference frame are from the compensating

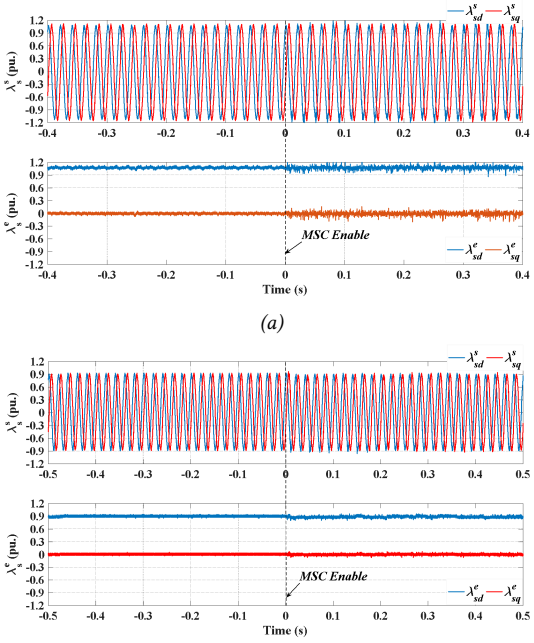

(a)

(b)

***Fig. 25**: Experimental Results Showing the Waveforms of the Stator Flux Linkage in the Stationary Reference Frame (Top) and the Stator Flux Reference Frame (Bottom) while Enabling the MSC with $i'^{e}_{rd} = 0$ (a) General dq-PLL and (b) DSOGI-PLL.*

voltages which is affected only by the stator magnetizing current as shown in equations (24) and (25) for each axis,

$$v^{e''}_{rd} = (1-\sigma)\tau_r \frac{d\left|\vec{i}^{\,e}_{ms}\right|}{dt}, \tag{24}$$

$$v^{e''}_{rq} = \omega_{sl}(1-\sigma)\tau_r \left|\vec{i}^{\,e}_{ms}\right|. \tag{25}$$

However, if the grid voltage is constant, only the q-axis component does appear. The PWM signals are generated from the command voltages, but they are not yet applied to the converter.

The 3rd Step: Before enabling the MSC by the actual PWM signals, the vector of the converter command voltage $\vec{v}^{\,r''}_{r}$ must coincide with the vector of the measured rotor voltage $\vec{v}^{\,'r}_{r}$. The misalignment between two vectors results in failure to start the converter. The misalignment occurs every time that the controller is reset although the initial rotor position correction was successfully performed. The reason for this misalignment is because the rotor position calculation is executed only when the Z-pulse appears resulting in initial rotor position correction. However, when starting the DFIM from standstill, there is no Z-pulse exist. The results proving this cause of the problem are shown in Fig. 17. The test is performed by manually rotating the rotor shaft of the DFIM and recording the necessary waveforms. This figure contains the waveforms of the d-axis converter

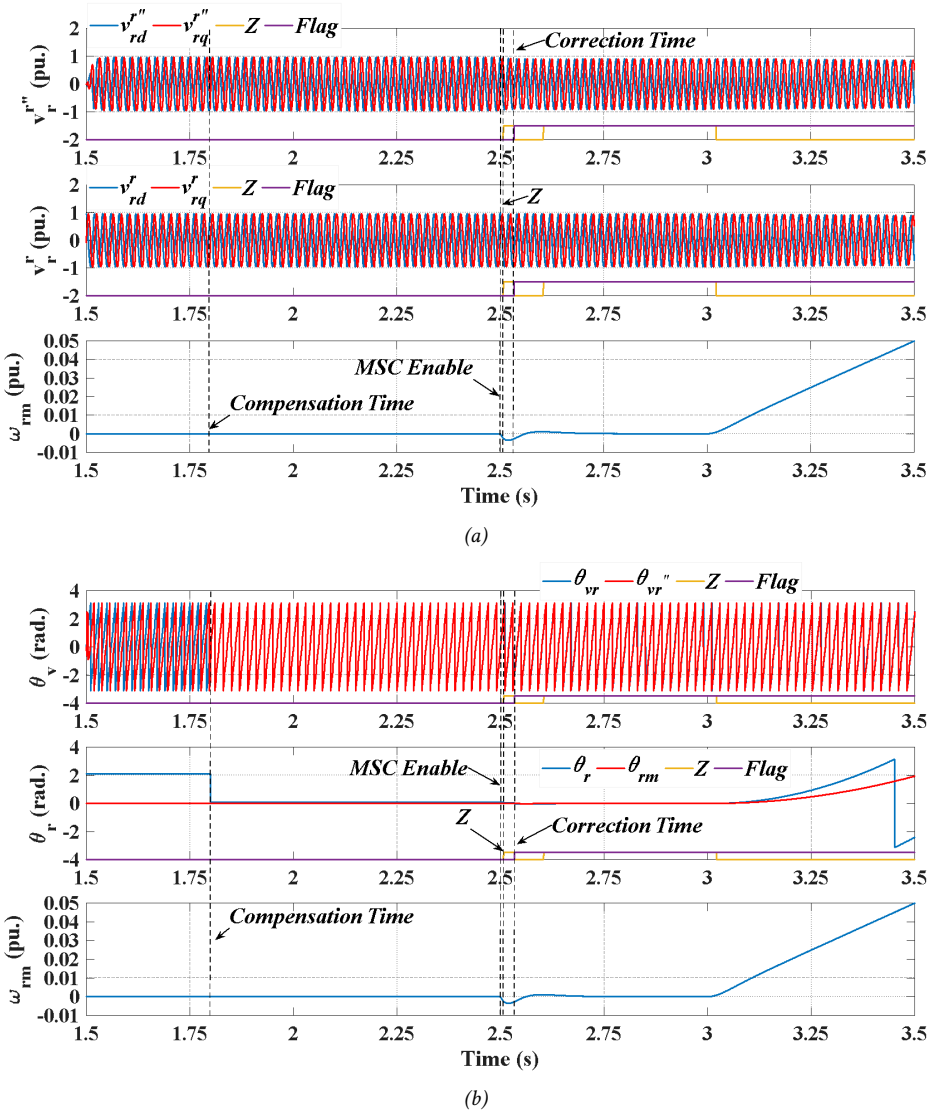

***Fig. 26**: Simulation Results Showing (a) the Group of the Rotor Voltage Waveforms and (b) the Group of the Necessary Position Relating to the Operation at Steps 3 and 4.*

command voltage, $v_{rd}^{r"}$ and the d-axis measured rotor voltage, $v_{rd}^{'r}$ in the rotor reference frame. Both are plotted at the top axis while the Z-pulse is plotted at the bottom axis. As shown in this figure, before appearance of the Z-pulse, the $v_{rd}^{r"}$ is not coincided with the$v_{rd}^{'r}$, but they are coincided just after the Z-pulse appears. Therefore, the compensation process must be performed before enabling the MSC.

The compensation process is achieved by comparing the position of $\vec{v}_r^{r"}$ to the position of $\vec{v}_r^{'r}$, as illustrated in Fig.16b, which results in an error rotor angle, $\Delta\theta_r$. The $-\Delta\theta_r$ is add to the measured θ_r for compensating the rotor position which results in an initial rotor angle,θ_{r0}.

The compensation results are illustrated in the waveforms of $v_{rd}^{'r}$ and $v_{rd}^{r"}$ shown in the top Fig. 18. The compensation flag is used to enable compensation process. The phase shift between $v_{rd}^{'r}$ and $v_{rd}^{r"}$ is arbitrary and it becomes zero immediately after the compensation process is enabled. At this stage, the MSC is now ready to operate, and the compensation angle must still be temporarily held until the first Z-pulse exists.

The 4^{th} Step: Following the 3^{rd} step, the MSC is enabled, and the waveform of $v_{rd}^{'r}$ contains the switching frequency component as shown in the top of Fig.19. Meanwhile, all controller reference signals must be changed back to the actual references. The speed reference is set to zero to maintain the rotor speed at standstill.

The 5^{th} Step: The speed reference is then ramped up and the rotor starts rotating. The compensation angle is still maintained until the Z-pulse exists, so the $\Delta\theta_r$ becomes zero and the compensation process is automatically terminated. The rotor position is the corrected following the existence of the Z-pulse. Meanwhile, the rotor accelerates to the final speed.

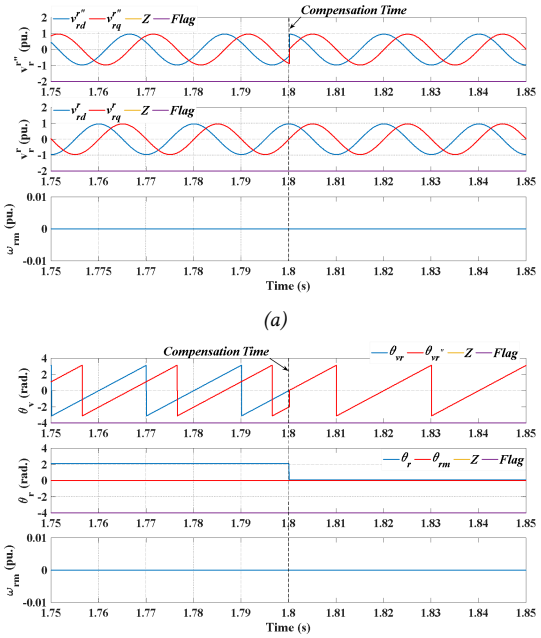

Fig. 27: Simulation Results Showing (a) the Group of the Rotor Voltage Waveforms and (b) the Group of the Necessary Position Relating to the Operation at Steps 3 and 4 during Compensation Process.

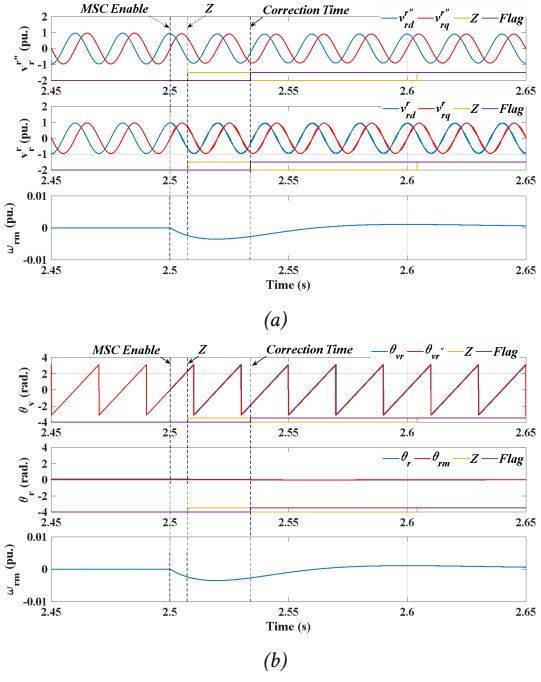

Fig. 28: Simulation Results Showing (a) the Group of the Rotor Voltage Waveforms and (b) the Group of the Necessary Position Relating to the Operation at Steps 3 and 4 during MSC Enable and Correction Processes.

4. SIMULATION AND EXPERIMENTAL SETUP

The computer simulations were performed to validate the proposed soft-start operation using PLECS software.

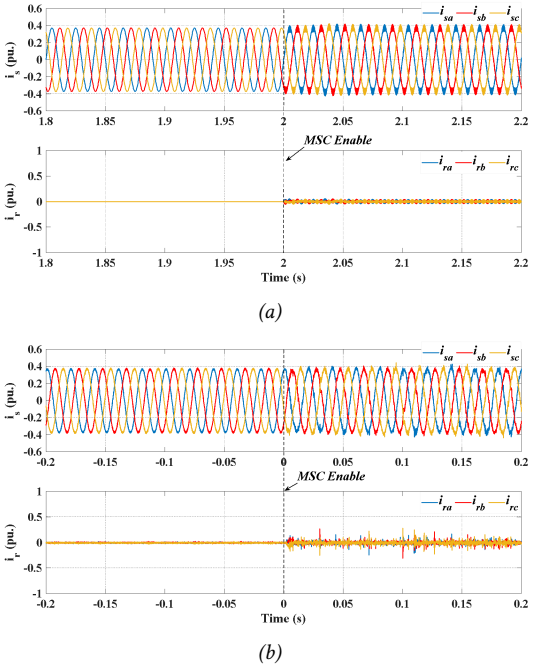

Fig. 29: (a) Simulation and (b) Experimental Results Showing the Waveforms of (Top) the Stator Current and (Bottom) the Rotor Current while Enabling the MSC with $i'^{e}_{rd} = 0$

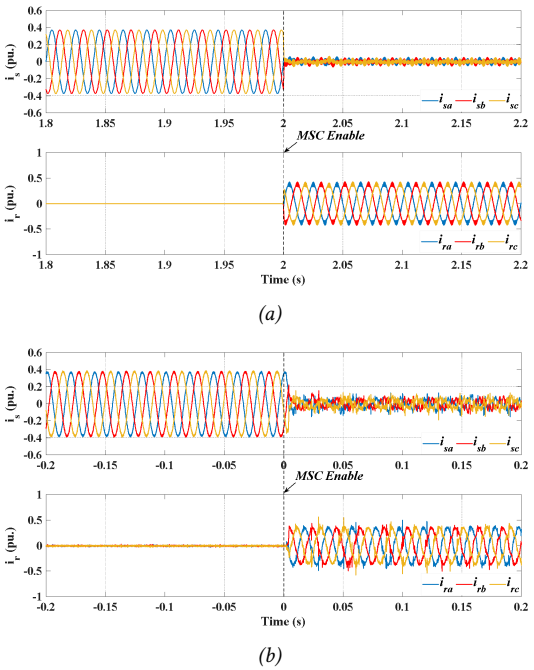

Fig. 30: (a) Simulation and (b) Experimental Results Showing the Waveforms of (Top) the Stator Current and (Bottom) the Rotor Current while Enabling MSC with $i'^{e}_{rd} = \left|\vec{i}^{\,e}_{ms}\right|$

The simulation was performed on a 5 kW wound rotor

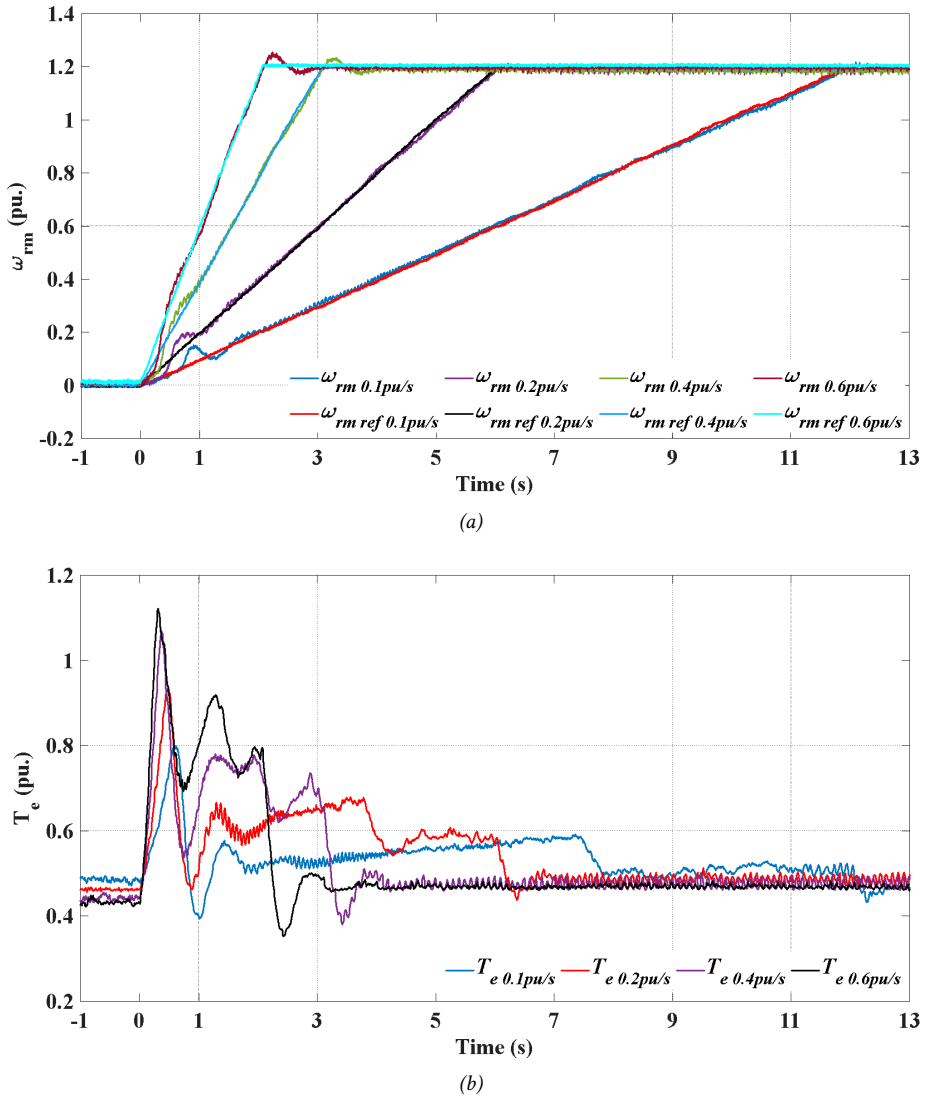

***Fig. 31**: Experimental Results Showing (a) the Waveforms of the Rotor Speed and (b) the Filtered Waveforms of the Electromagnetic Torque while Accelerating with the 0.5 pu. Load at 0.1 pu./s, (b) 0.2 pu./s, (c) 0.4 pu./s and 0.6 pu./s Ramp Rates in the Same Windows.*

induction machine having the variables and parameters as shown in Table 2. The parameters were acquired from the standard test procedures such as VI method, no-load test and locked rotor test. However, due to the WRIM structure, the no load and locked rotor test were replaced by open-circuited and short-circuited tests respectively.

The stator of the DFIM is supplied by a 400V 50 Hz three-phase source. The simulations were performed using PLECS software as depicted in Fig. 20. The results were plotted using MATLAB software. The MSC is controlled with the sampling rate at 10 kHz, while the switching frequency is set to 5 kHz. As a result, the PWM signal is updated twice for each switching period. The simulation was performed based on C-Script as applied in the actual system. The algorithm and code are directly adopted to the microcontroller with little modification.

The experiments were performed following an experimental diagram depicted in Fig. 21, while the actual system is shown in Fig.22. The STM32F407 Discovery Board is used in this research. The reference is setup on the laptop with communication via RS485 with the microcontroller. The WRIM is mechanically coupled to a 7.5 kW squirrel cage induction motor (SCIM) driven by a commercial AC Drive. The SCIM is driven under sensorless torque-controlled mode.

The DC bus of the MSC is supplied by the three-phase diode bridge rectifier for simplicity. Moreover, during the operation in sub-synchronous speed region, the rotor power is dissipated in the dynamic braking circuit. Therefore, the DFIM can operate in all speed regions. The experiments were performed under several conditions according to the flowchart in Fig.15. The results are shown and discussed in the next section.

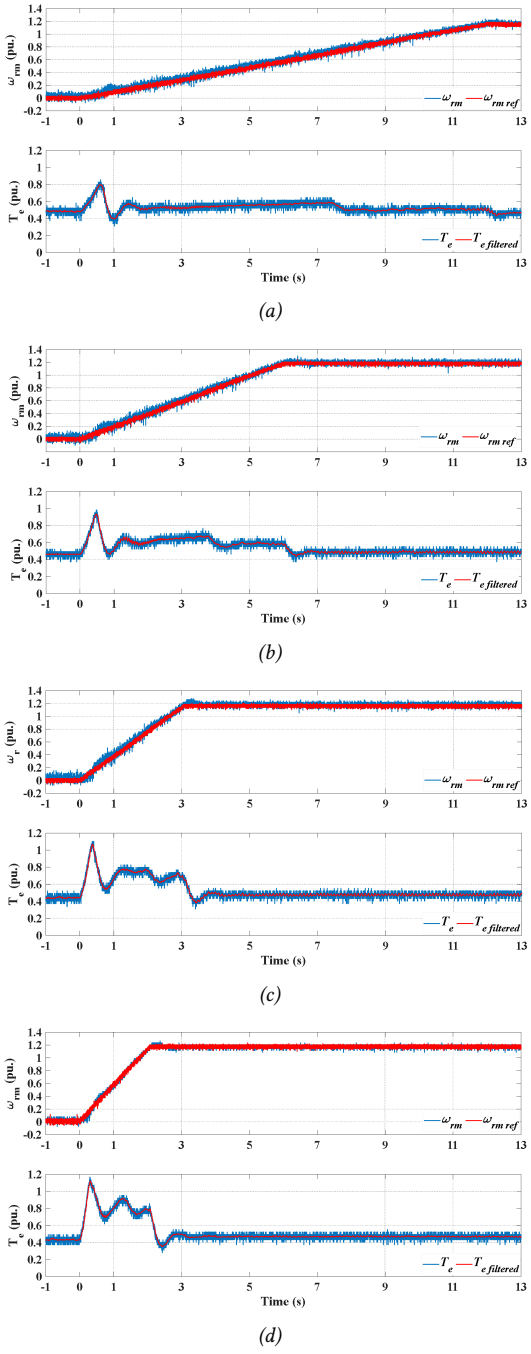

***Fig. 32**: Experimental Results Showing the Waveforms of (Top) the Reference Speed and Actual Speed of the Rotor and (Bottom) the Electromagnetic Torque while Accelerating with the 0.5 pu. Load at (a) 0.1 pu./s, (b) 0.2 pu./s, (c) 0.4 pu./s and 0.6 pu./s Ramp Rates.*

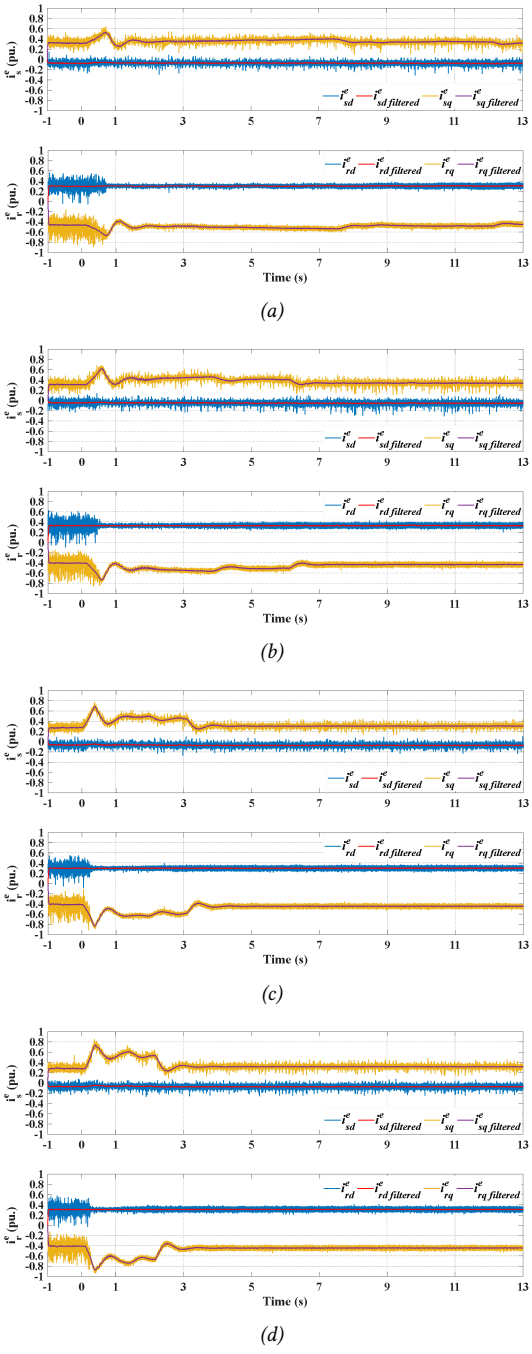

***Fig. 33**: Experimental Results Showing the Waveforms of (Top) the Stator Current and (Bottom) the Rotor Current in the Stator Flux Reference Frame during Acceleration with the 0.5 pu. Load at (a) 0.1 pu./s, (b) 0.2 pu./s, (c) 0.4 pu./s and 0.6 pu./s Ramp Rates.*

5. SIMULATION AND EXPERIMENTAL RESULTS

In this section, the simulation and experimental results are presented. The detail starts from the comparison between the simulation results and the experimental results during operation at step 1 and step 2. Operation at steps 3 and parts of step 4 are discussed and depicted in the simulation results to enhance understanding in the problem of initial rotor position correction. It is a vital step prior connecting the MSC to the rotor circuit. The results during acceleration are then presented and only the experimental results are presented and discussed in detail. The results start from the waveforms of the necessary variables at different ramp rates. They are plotted in both separate and single frames for comparison purposes. The final set of the results are the stator

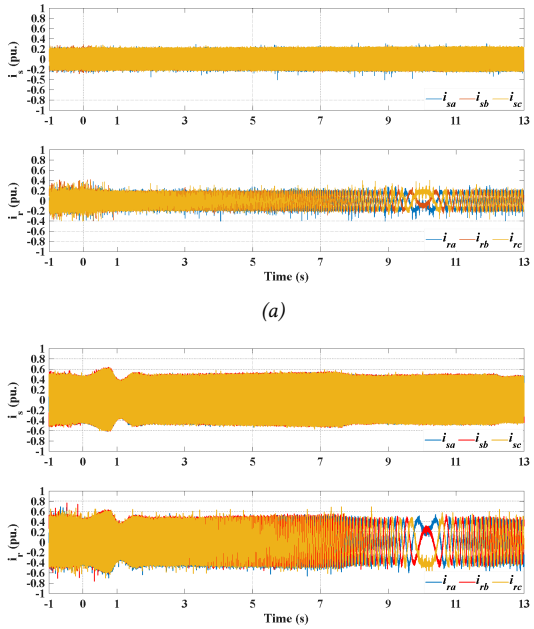

(a)

(b)

***Fig. 34**: Experimental Results Showing the Waveforms of (Top) the Three-Phase Stator Current and (Bottom) the Rotor Current during Acceleration under (a) No-load and (b) 50% Load Conditions with* $i'^{e}_{rd} = 0.5\left|\vec{i}^{\,e}_{ms}\right|$.

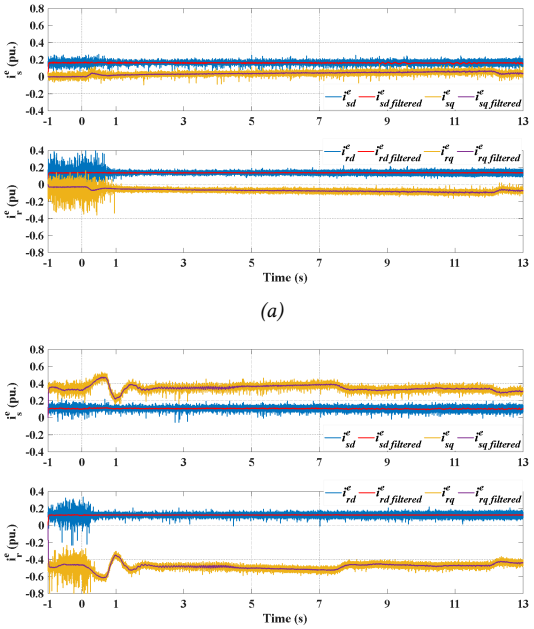

(a)

(b)

***Fig. 35**: Experimental Results Showing the Waveforms of (Top) the Stator Current and (Bottom) the Rotor Current in the Stator Flux Reference Frame during Acceleration under (a) No-load and (b) 50% Load Conditions with* $i'^{e}_{rd} = 0.5\left|\vec{i}^{\,e}_{ms}\right|$.

and rotor current waveform while operating the DFIM without and with the DSOGI-PLL applied to the stator flux estimation process.

First, the results start from stator connection in Fig. 23 followed by the stator flux vector estimation in Fig.24. Fig.23b shows that there are high inrush currents while connecting the stator to the grid. The inrush currents from the experimental results are significantly higher than those from the simulation results. This difference is because the saturation is not included in the slip-ring motor model in the simulation [38]. The results shown in Fig. 24 are waveforms of the stator flux during start of the stator flux vector estimation. The comparison proves that the model can be used to simulate the actual system.

The results shown in Fig. 25 are the stator flux estimated waveforms while $i'^{e}_{rd} = 0$ using different phase locked loop schemes for angular velocity and position estimation, the general dq-PLL and the DSOGI-PLL. The oscillation is prominent while using the general dq-PLL because both positive and negative sequence components are fed to the PLL. However, in the case of using DSOGI-PLL, only the positive sequence component is extracted and fed to the PLL, so the oscillation due to unbalanced voltage disappeared.

The simulation results for operation at steps 3-5 are shown in Figs. 26-28. Fig. 26 shows the results in the whole period of the operation at these steps. The simulation was performed by setting the initial mechanical rotor position to zero while the measured rotor

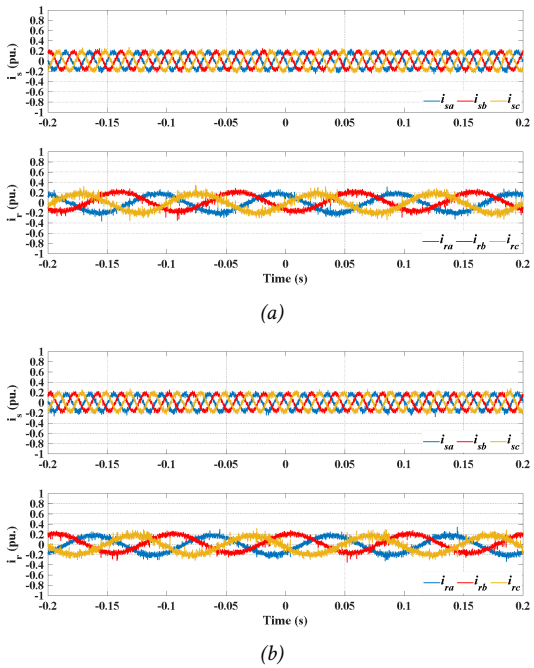

(a)

(b)

***Fig. 36**: Experimental Results Showing the Waveforms of (Top) the Stator Current and (Bottom) the Rotor Current under No-Load Condition (a) with the General dq-PLL and (b) with the DSOGI-PLL.*

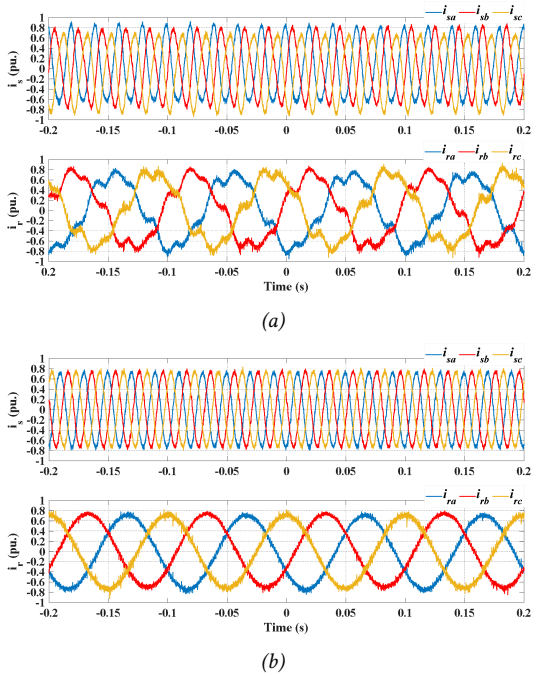

***Fig. 37**: Experimental Results Showing the Waveforms of (Top) the Stator Current and (Bottom) the Rotor Current under No-Load Condition (a) with the General dq-PLL and (b) with the DSOGI-PLL.*

position error was set to $\pi/3$ radians leading. Therefore, converting to electrical value, the measurement error becomes $2\pi/3$ radians. Starting from the time 1.5 s. the stator flux estimation was initiated, and the rotor position compensation was performed at the time 1.8 s. Focusing on Figs. 27a, the waveforms of the $v_r^{r"}$, which are the command voltage for the MSC, are not in-phase with the v_r^r, which are the rotor terminal voltage. It can also be observed on the waveforms of Fig. 27b that the angles of both voltages are mismatched. Considering the middle waveform of Fig. 27b, the measured electrical rotor angle is higher than actual rotor angle for $2\pi/3$ radians.

As discussed in Section 3, The compensation occurs at the time 1.8s, the waveforms of the $v_r^{r"}$ are in-phase with the v_r^r as shown in Fig 26a, as well as their positions as shown in Fig.26b. Therefore, the θ_r is close to θ_{rm}as shown in the middle of Figs 26b and 27b. The MSC is enabled at the time 2.5 s., meanwhile, there is a change in the rotor speed as shown in the bottom of Figs 26a and 26b. causing a change in the rotor position. The magnified view during this interval is shown in Fig.28. In this case, the rotor position changes until the z-pulse appears, so the correction of the rotor position is performed at the time that the correction flag appears, which is the falling edge of the Z-pulse, causing the error angle to be zero. Meanwhile, the compensation process automatically stops due to disappearance of the error angle. The DFIM is now ready to be operated and starts accelerating at the time 3 s.

The results shown in Figs. 29 and 30 are the stator current and rotor current waveforms while enabling the MSC under different d-axis rotor current reference. The simulation results do match the experimental results, so the simulation model can be used to simulate the operation of the actual system under this process. However, rotor current waveforms in Fig. 29b and 30b are polluted due to the noise interfering with the measured signal.

Figs. 31 and 32 show the waveform of the speed and the electromagnetic torque during acceleration from stand still to 1.2pu. at different ramp rates, 0.1 pu./s, 0.2 pu./s, 0.4 pu./s, and 0.6 pu./s. In this experiment $i'^{e}_{rd}$is set to $\left|\vec{i}^{e}_{ms}\right|$ The results in Fig.31 are plotted in the same windows for ease of comparison for the torque waveforms. The same results are plotted separately as shown in Fig. 32.

Fig. 33 shows the stator and rotor current waveforms in the stator flux reference frame. The value of $i^e_{sd}$is always zero as the DFIM is magnetized via the rotor only. The DFIM can successfully accelerate and continue to operate at the final speed. The accelerating torque is proportional to the ramp rate. Moreover, the operation at standstill is not the problem as the torque waveform during such interval is steady.

The results shown in Fig.34 are the stator and rotor current waveforms in their three-phase reference frame. It can be investigated from the rotor current waveforms that the phase sequence is changed while the DFIM accelerates through synchronous speed. The experimental results in Fig.35 are the stator and rotor current waveforms in stator flux reference frame. The results in this form show that the DFIM is in under excitation mode, so it is magnetized via both stator and rotor circuits.

The last set of the experimental results are the stator and rotor current waveforms while using different stator flux estimation schemes, general dq-PLL and DSOGI-PLL. They are shown in Fig. 36 for no-load condition and Fig. 37 for full load condition. Under no-load condition, the effect of unbalance voltage source is insignificant. However, the effect of unbalanced voltage is significant when the DFIM is operating at full load as shown in Fig. 37a. It results in unbalanced stator currents and distortion in the rotor current waveforms. However, if the DSOGI-PLL is applied to estimate the stator flux, the effect of unbalanced is significantly reduced as shown in Fig. 37b.

6. CONCLUSIONS

This paper presents the system implementation of the proposed soft start method from standstill for a DFIM based on conventional topology. Neither circuit reconfiguration nor change of the control method is required. The paper begins with a brief review of the existing methods followed by a short discussion about the theory in Section 2. The DSOGI-PLL is applied to this research for position and speed estimation of the stator flux vector to prevent the effect of grid voltage imbalance. The controller design is also discussed in this

section. The series PI controller structure is selected for ease of locating the pole and zero of each controller. The bandwidth of the current loop is adjusted to be much higher than that of the speed loop as generally applied to the cascaded control of the electric drive. The details of the proposed soft-start method are discussed in Section 3, where the operating procedure is arranged and presented in the flowchart followed by the graphical explanation.

The simulations were performed using PLECS software and the simulation results are plotted using MATLAB software. The experiment was set up and the STM32F407 Discovery board is the main processor to control the DFIM. The experimental results were recorded and plotted using MATLAB software.

The simulation and experimental results are classified based on the operating steps. They begin with operation in steps 1 and 2. The waveforms of the stator currents while connecting the stator to the grid are illustrated. It should be noted that the inrush current is significantly high in the experimental result. The inrush current is due to saturation in the magnetic core of the WRIM. It does not occur in the simulation results because the magnetic saturation is not included in the WRIM model. This inrush current is only the main drawback of the proposed method. However, for the large WRIM, several inrush reduction methods applied to the three-phase transformer can also be applied to the operation at this step.

The process of estimating the stator flux linkage was then performed. The stator flux linkage waveforms from both simulation and experiment are presented and they are nearly identical. As discussed, the DSOGI-PLL is applied for position and speed estimation of the stator flux. The waveforms of the stator flux estimated using the general dq-PLL and DSOGI-PLL are shown in Fig. 25. The effect of voltage imbalance significantly appears on the stator flux waveform while using the general dq-PLL, and it disappears while using the DSOGI-PLL.

The simulation for the operation in step 3 was performed to explain the problem that occurs when enabling the MSC. As discussed in Section 3, the correct rotor position cannot be estimated until the first index pulse appears. Consequently, the converter voltage and the rotor voltage are mismatch resulting in failure to enable the MSC. Therefore, the rotor position compensation must be performed by comparing the vector of the controller output to the measured rotor voltage vector. The compensation process stopped immediately after the Z-pulse existed. The simulation results are illustrated in Figs.26 -28.

Theoretically, the DFIM can be magnetized via either stator or rotor circuit. It can be substantiated by the results shown in Figs. 29 and 30. After enabling the MSC, the speed command is set to zero, leading to zero q-axis rotor current. If $i^e_{rd}$is set to zero, the DFIM is magnetized via the stator circuit only as depicted in Fig.29. Conversely, if $i^e_{rd}$is set to $\left|\vec{i}^{\,e}_{ms}\right|$, the DFIM is magnetized via the rotor circuit only as depicted in Fig.30.

Once the MSC is enabled, the DFIM is ready to be accelerated. The experiments during acceleration from a standstill to the super-synchronous speed region at 1.2 pu. speed were performed. The experimental results at different ramp rates are plotted together in the same windows for comparison. Moreover, the individual ramp rate results are also presented. In this experiment, the value of $i^e_{rd}$is set to $\left|\vec{i}^{\,e}_{ms}\right|$, so the DFIM is magnetized via the rotor only. The power factor of the stator is unity because the value of i^e_{sd} remains zero throughout these experiments, which substantiate the theory of reactive power control of the DFIM.

The stator and rotor current waveforms under no-load condition are also presented and compared to the waveforms under 50% load condition. The results are shown in their own three-phase reference frames and stator flux reference frame. Under no-load condition, the steady-state current at 1.2pu. speed is slightly higher than the current at standstill due to the viscous friction which is proportional to the operating speed.

The effects of grid voltage imbalance are also presented in the last set of the experimental results. The effects on the stator and rotor currents are not significant while operating at no-load. However, they drastically distort the rotor current waveforms while operating at full load. This effect has been suppressed when the DSOGI-PLL is applied.

Finally, it can be concluded that the proposed soft start method can successfully be applied to operate the DFIM from a standstill to any speed region without either circuit reconfiguration or change in control method, as proved by both simulation and experimental results. The only drawback of this method is the inrush current when connecting the stator to the grid . However, it is minor if the existing method to mitigate the inrush current for the transformer is applied.

REFERENCES

[1] W. Leonhard. *Control of Electrical Drives*, 3rd ed. Berlin, Germany: Springer, 2001.

[2] P. Vas. *Vector Control of AC Machines*, UK: Oxford University Press, 1990

[3] R. Pena, J. C. Clare, and G. M. Asher, "Doubly-Fed Induction Generator Using Back-to-Back PWM Converters and Its Application to Variable Speed Wind-Energy Generation", *IEE Proceeding of Electric Power Applications*, vol. 143, no. 5, pp. 380-387, 1996.

[4] G. Tapia, G. Santamaria, M. Telleria, and A. Susperregui, "Methodology for Smooth Connection of Doubly Fed Induction Generators to the Grid," *IEEE Transactions on Energy Conversion*, vol. 24, no. 4, pp. 959-971, Dec 2009.

[5] S. Muller, M. Deicke, and R. W. De Doncker, "Doubly Fed Induction Generator Systems for Wind

Turbines," *IEEE Industry Applications Magazine*, vol. 8, no. 3, pp. 26–33, May.-Jun. 2002.

[6] B. Wu, Y. Lang, N. Zargari, and S. Kouro. *Power Conversion and Control of Wind Energy Systems*. Hoboken, NJ, USA: Wiley, 2011.

[7] M. Debbou, A. Damdoum, and M. P.-David, "Optimal Sliding Mode Control for DFIM Electric Marine Thruster," in *Proceedings of the International Conference on Electrical System for Aircraft, Railway, Ship Propulsion and Road Vehicles & International Transportation Electrification Conference (ESARS-ITEC)*, Nov. 2016, pp. 1–6.

[8] Y. Pannatier, B. Kawkabani, C. Nicolet, A. Schwery and J. . -J. Simond, "Start-Up and Synchronization of a Variable Speed Pump-Turbine Unit in Pumping Mode," in *The XIX International Conference on Electrical Machines - ICEM 2010*, Rome, Italy, 2010, pp. 1-6.

[9] Y. Pannatier, B. Kawkabani, C. Nicolet, J. -J. Simond, A. Schwery and P. Allenbach, "Investigation of Control Strategies for Variable-Speed Pump-Turbine Units by Using a Simplified Model of the Converters," *IEEE Transactions on Industrial Electronics*, vol. 57, no. 9, pp. 3039-3049, Sept. 2010.

[10] X. Yuan, J. Chai, and Y. Li, "A Converter-Based Starting Method and Speed Control of Doubly-Fed Induction Machine With Centrifugal Loads," *IEEE Transaction on Industry Applications*, vol. 47, no. 3, pp. 1409–1418, May/Jun. 2011.

[11] Y. Pannatier, B. Kawkabani, C. Nicolet, A. Schwery and J. . -J. Simond, "Optimization of the Start-Up Time of a Variable Speed Pump-Turbine Unit in Pumping Mode," in *2012 XXth International Conference on Electrical Machines*, Marseille, France, 2012, pp. 2126-2132.

[12] T. Maendly, A. Hodder and B. Kawkabani, "Start-Up of a Varspeed Group in Pump Mode, Practical Implementations and Tests," in *2016 XXII International Conference on Electrical Machines (ICEM)*, Lausanne, Switzerland, 2016, pp. 1201-1207.

[13] A. Joseph, R. Selvaraj, T. R. Chelliah, and S.V. Appa Sarma, "Starting and Braking of Large Variable Speed Hydrogenerating Unit Subjected to Converter and Sensor Faults," *IEEE Transactions on Industry Applications*, vol. 54, no. 4, pp. 3372–3382, Jul.-Aug. 2018.

[14] T. Zhao, D. Xiang and, and Y. Sheng, "An Approach to Start a Shaft Generator System Employing DFIM under Power Take Me Home Mode," in *2018 IEEE International Power Electronics and Application Conference and Exposition (PEAC),* Shenzhen, China, 2018, pp. 1-5.

[15] J. Zhao, H. Li, X. Xiang and W. Li, "Research on Startup and Emergency Braking Strategy of Doubly-Fed Induction-Machine-Based Flywheel Energy Storage System," in *2023 26th International Conference on Electrical Machines and Systems (ICEMS)*, Zhuhai, China, 2023, pp. 4971-4976.

[16] M. Narayanasamy and Y. Sukhi, "Rotor Short Circuited Start-up Strategy for a Doubly-Fed Induction Machine-fed Large-Variable-Speed Pumped Storage Unit Operating in Pumping Mode," *Journal of Power Electronics,* vol. 23, pp. 1733–1744, 2023.

[17] A. Banerjee, M. S. Tomovich, S. B. Leeb, and J. L. Kirtley, "Control Architecture for a Switched Doubly Fed Machine Propulsion Drive," *IEEE Transactions on Industry Applications*, vol. 51, no. 2, pp. 1538–1550, Mar-Apr. 2015.

[18] A. Banerjee, M. S. Tomovich, S. B. Leeb and J. L. Kirtley, "Power Converter Sizing for a Switched Doubly Fed Machine Propulsion Drive," *IEEE Transactions on Industry Applications,* vol. 51, no. 1, pp. 248-258, Jan.-Feb. 2015.

[19] T. Kawabata, Y. Kawabata, and K. Nishiyama, "New Configuration of High-Power Inverter Drives," in *Proceedings of IEEE International Symposium on Industrial Electronics*, Warsaw, Poland, vol. 2, 1996, pp. 850–855.

[20] Y. Kawabata, E. C. Ejiogu, K. Nishiyama and T. Kawabata, "High-Power Drive Using a Wound Rotor Induction Motor and Two Current Controlled Inverters," in *Proceedings of Power Conversion Conference - PCC '97*, Nagaoka, Japan, vol. 2, 1997, pp. 579-582.

[21] Y. Kawabata, E. Ejiogu, and T. Kawabata, "Vector-Controlled Double Inverter-Fed Wound-Rotor Induction Motor Suitable for High-Power Drives," *IEEE Transactions on Industry Applications*, vol. 35, no. 5, pp. 1058–1066, Sep.-Oct. 1999.

[22] G. Poddar and V. T. Ranganathan, "Sensorless Field-Oriented Control for Double-Inverter-Fed Wound-Rotor induction motor drive," *IEEE Transactions on Industrial Electronics*, vol. 51, no. 5, pp. 1089–1096, Oct. 2004.

[23] G. Poddar and V. T. Ranganathan, "Direct Torque and Frequency Control of Double-Inverter-Fed Slip-Ring Induction Motor Drive," *IEEE Transactions on Industrial Electronics*, vol. 51, no. 6, pp. 1329-1337, Dec. 2004.

[24] F. Bonnet, P. -E. Vidal, and M. Pietrzak-David, "Dual Direct Torque Control of Doubly Fed Induction Machine," *IEEE Transactions on Industrial Electronics,* vol. 54, no. 5, pp. 2482-2490, Oct. 2007.

[25] Y. Liu and L. Xu, "The Dual-Current-Loop Controlled Doubly Fed Induction Motor for EV/HEV Applications," *IEEE Transactions on Energy Conversion*, vol. 28, no. 4, pp. 1045–1052, Dec. 2013.

[26] M. Abdellatif, M. Debbou, I. S.-Belkhodja, and M. P. David, "Simple Low-Speed Sensorless Dual DTC for Double Fed Induction Machine Drive," *IEEE Transactions on Industrial Electronics*, vol. 61, no. 8, pp. 3915–3922, Aug. 2014.

[27] V. V. Reddy, N. Aarzoo, G. Poddar and S. Sau, "Improved Sensorless Operation of Double Inverter Fed Wound Rotor Induction Machine with Seamless Mode Transitions," *IEEE Transactions on*

Industrial Electronics, vol. 70, no. 11, pp. 11078-11086, Nov. 2023.

[28] L. S. Barik and H. Misra, "Dual Side Field Oriented Control of Slip Ring Induction Motor," *IEEE Transactions on Industrial Electronics*, Early Access, May. 2024.

[29] A. Nanda and V. S. S. P. K. Hari, "Dual Volts-per-Hertz Control of Double-Inverter-Fed Wound Rotor Induction Machine," *IEEE Transactions on Industrial Electronics*, vol. 71, no. 3, pp. 2198–2207, Mar. 2024.

[30] A. Nanda and V. S. S. P. K. Hari, "Improved Dual Volts-Per-Hertz Control of Double Inverter-Fed Wound Rotor Induction Machine," *IEEE Transactions on Industrial Electronics*, vol. 71, no. 9, pp. 10268-10276, Sept. 2024.

[31] Y. Zhang and B. T. Ooi, "Adapting DFIGs for Doubly-Fed Induction Motors Operation," in *2012 IEEE Power and Energy Society General Meeting*, San Diego, CA, USA, 2012, pp. 1-8.

[32] M. Bodson and M. A. Hossain, "Integrated Control of a Motor/Generator Set Composed of Doubly Fed Induction Machines," *IEEE Journal of Emerging and Selected Topics in Power Electronics*, vol. 8, no. 2, pp. 1858-1869, June 2020.

[33] G. peng, K.Ni, C.Gan, R. Qu, and Y. Hu, "A Direct Starting Method of Doubly-Fed Induction Machine for Shipboard Propulsion System Application," in *2021 24th International Conference on Electrical Machines and Systems (ICEMS)*, Gyeongju, Korea, Republic of, 2021, pp. 949-954.

[34] Patrick L. Jansen and Robert D. Lorenz, "A Physical Insightful Approach to the Design and Accuracy Assessment of Flux Observers for Field Oriented Induction Machine Drives," *IEEE Transactions on Industry Applications*, vol. 30, No. 1, pp. 101-110, Jan.-Feb 1994.

[35] Cristian Lascu, Ion Boldea, and Frede Blaabjerg, "A Modified Direct Torque Control for Induction Motor Sensorless Drive," *IEEE Transactions on Industry Applications*, vol. 36, no. 1, pp. 122-130, Jan.-Feb 2000.

[36] Z. Ali, N. Christofides, L. Hadjidemetriou, E. Kyriakides, Y. Yang and F. Blaabjerg, "Three-phase Phase-Locked Loop Synchronization Algorithms for Grid-Connected Renewable Energy Systems: A Review," Renewable and Sustainable Energy Reviews, vol. 90, pp. 434-452, July 2018.

[37] D. Wilson, "Teaching Your PI Controller to Behave," TI Technical Article, July 2015.

[38] PLECS User Manual Version 4.8, *Plexim GmbH,* 2002-2024.

Knapoj Chaimanekorn received the B.Eng in Electrical Engineering with first class honors from King Mongkut's Institute of Technology Ladkrabang, Thailand in May 2024. His research interests include power electronics and AC drives, high performance drive systems, modeling and control of electrical machines.

Warachart Suwan-ngam received the B.Eng. and M.Eng. in Electrical Engineering from the King Mongkut's Institute of Technology Ladkrabang (KMITL), Bangkok, Thailand in 1999 and 2002, respectively, and the Ph.D. in Electronic and Electrical Engineering from the University of Strathclyde, Glasgow, UK. in 2008. He is currently an Assistant Professor in the Department of Electrical Engineering, School of Engineering, KMITL. His research interests include electrical machines and AC drives, power electronics applications for renewable energy, condition monitoring and fault diagnosis for electrical machines and power converters, and DSP applications for AC drives and power electronics converters.